

## HRTEM IMAGE FILTRATION: NANOSTRUCTURAL ANALYSIS OF A PILLARED CLAY

CHRISTIAN CLINARD<sup>1</sup>, TUSHAR MANDALIA<sup>1</sup>, DENISE TCHOUBAR<sup>2</sup> AND FAIZA BERGAYA<sup>1,\*</sup>

<sup>1</sup> Centre de Recherche sur la Matière Divisée, CNRS-Université d'Orléans, 1b, rue de La Férolle, 45071 Orléans Cedex 2, France

<sup>2</sup> CRT Plasma Laser, 14 rue d'Issoudun - B.P 6744 45067 Orléans Cedex 2, France

**Abstract**—Nanostructural analysis of pillared clay samples using high-resolution transmission electron microscopy has been developed. Montmorillonite samples were pillared using partially hydrolyzed Al and Fe solutions. Two samples, M01 and M05, corresponding to Fe/(Fe+Al) ratios of 0.1 and 0.5, respectively, were analyzed. The different steps of image filtration, resulting from filtration by ring-shaped masks, are illustrated and discussed from lattice imaging of sample M01. This procedure is used to show the heterogeneous distribution of the basal spacings in the different ordered domains. Domains of mesoporosity and distribution of the different Fe species are studied specifically in the sample M05. The quantitative HRTEM results are discussed and compared with X-ray diffraction patterns obtained from the same sample.

**Key Words**—Fe Pillared Clay, High-resolution Transmission Electron Microscopy, Image Analysis, Mesoporosity.

### INTRODUCTION

The microstructural analysis of materials using a filtration technique of images obtained from high-resolution transmission electron microscopy (HRTEM), was developed several years ago with particular reference to layered materials. This technique can reveal ordered structures coexisting with disordered and/or amorphous domains. Powerful analysis algorithms allow the determination of a certain number of quantitative parameters specific to each material (Bergaya *et al.*, 1996; Douce *et al.*, 1999; Sharma *et al.*, 1999; Rouzaud *et al.*, 1999; Clinard *et al.*, 2001; Rouzaud and Clinard, 2003). These parameters can then be correlated with properties obtained from other techniques such as X-ray diffraction (XRD), spectroscopic methods and thermal analysis.

Mixed Al-Fe pillared clays have not been investigated extensively and their structures are not well understood. However, they may have important applications in catalysis (d'Emmerez *et al.*, 1987) and in developing clay/polymer nanocomposites with promising firing properties (Fompérie *et al.*, 2000, 2001). X-ray diffraction patterns of these samples show a peculiar low-angle peak (Mandalia *et al.*, 1998) which could be interpreted as large interlayer repeat distances. However, questions arise about what kind of Fe species are responsible for these large distances, and whether these values correspond to the interlayer distances.

In this study we have applied the filtration technique of the 2D image Fourier transform to analyze these structural characteristics of HRTEM images.

\* E-mail address of corresponding author:  
f.bergaya@cnrs-orleans.fr

DOI: 10.1346/CCMN.2003.0510408

### MATERIALS AND METHODS

#### *Pillaring of montmorillonite*

A sample of Wyoming montmorillonite was pillared with a solution of partially hydrolyzed Fe and Al hydroxide (Bergaya, 1990; Mandalia *et al.*, 1998, 2003). The pillared clays show unusual XRD patterns (Figure 1), notably the presence of a prominent peak corresponding to mean distances varying from 5 to ~8 nm depending on the Fe/(Fe+Al) ratio in the pillaring solution. This shows a structure quite different from the same clay pillared only with partially hydrolyzed Al salt solutions, where only one diffraction peak corresponding to a basal spacing of 1.8 nm is observed (Figure 1). This peak is characteristic of the intercalation of Al<sub>13</sub> oligomer into the clay (Mandalia *et al.*, 1998). The pillared samples obtained by mixing partially hydrolyzed Fe and Al salt solutions with the clay, have structures which are much more complex and require HRTEM study. For TEM studies, two samples of pillared clays were used, corresponding to two Fe/(Al+Fe) ratios in the pillaring solutions of 0.1 and 0.5, respectively, designated M01 and M05. The distances observed at 5.2 nm and 7.2 nm, respectively, for the two samples are shown in Figure 1 (Mandalia *et al.*, 1998).

#### *Sample preparation for TEM studies*

In order to obtain a picture which minimizes the superposition of information, it is necessary to make very thin sections of the sample, prepared from an oriented deposit of the pillared clay embedded in an acrylic resin (L.R. White). The TEM observations were performed on slices ~50 nm thick obtained by using an ultramicrotome (Reichert ultracut) equipped with a diamond knife (Drukker).

The microscope used was a Philips CM20 type operating at 200 kV. Optic adjustments are obtained by using a low-dose camera.

#### Digitization of TEM micrographs

This work focuses on the structure determination of the pillared clay sample M05 which yields a peak distance of 7.2 nm.

The sample M01 served as a model because it includes extended well ordered structures which illustrate the different steps of the analytical method. A lattice image of this sample is shown in Figure 2. The digitization was performed with an AGFA scanner (Duoscan type) allowing the treatment of silver negatives. The digitized zone was  $1024 \times 1024$  pixels in size with a resolution of 2000 pixels per inch (ppi) which can be extended to 4000 ppi by interpolation. To calibrate the pixels in Å (or nm), a standard sample image was recorded under the same experimental conditions. Another clay mineral sample (kaolinite) was used as reference with a basal spacing of 0.72 nm.

Inhomogeneities often present in the observation area are related to: the development of the TEM picture; changes in lattice image with thickness and tilt of the clay particle; and non-uniformity of gray level along the lattice fringes due to changes of orientation of some parts of the layers.

The digitized image is therefore processed by a filtration technique. This procedure includes three steps: (1) reduction of noise corresponding to frequencies which are not related to the structure of the object but which arise from the inhomogeneities mentioned above; (2) identification of the different structure scales; and

(3) analysis and quantification of the characteristic structural parameters of this sample.

#### 2D Fourier transform and noise filtration

The digitized lattice image of sample M01 (Figure 2) shows large well ordered layer domains alternating with blurred zones containing dislocation clusters. Furthermore, there is no evidence that the periodicities in the various domains are the same across the whole image.

Figure 3 displays the first steps of the process from which the different periodic structures may be extracted from the image. The 2D Fourier transform yields two images: (1) the phase image, not shown here because it is not visually meaningful; and (2) the amplitude image modulus 'mo' (Figure 3a) which is equivalent to the square root of the intensity which would be diffracted by the sample. It contains diffraction spots related to the periodic order of the structure.

The profile of the gray level distribution (Figure 3b) is determined along a straight line joining the 'mo' image center to the diffraction spots. The central peak in this plot has been truncated. The  $x$  axis of the plot is the number of pixels, but it will be further calibrated as the wave vector modulus  $q$  (in  $\text{Å}^{-1}$  or in  $\text{nm}^{-1}$ ) by comparing it with the curve arising from the kaolinite standard. For this sample, the position of the 001 reflection in the same graph is:

$$q_{001} = 8.8 \text{ nm}^{-1} = 102 \text{ pixels}$$

in which  $q = 2\pi/d_{001}$  and  $d_{001} = 0.716 \text{ nm}$ .

The resulting value for a pixel on the  $x$  axis is:

$$1 \text{ pixel} = \delta q = 8.6 \times 10^{-2} \text{ nm}^{-1}$$

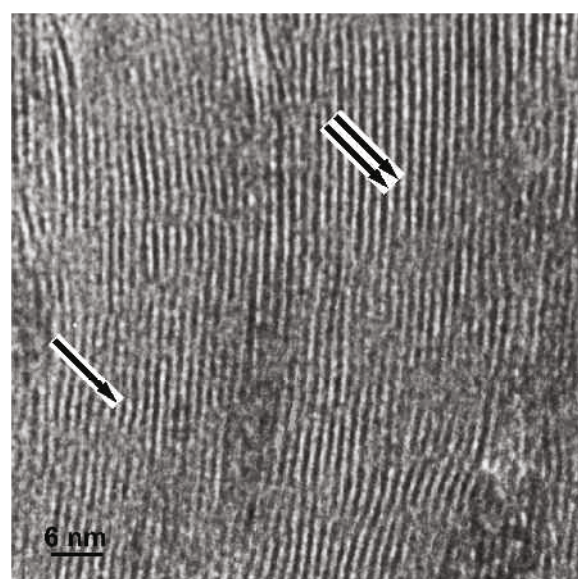


Figure 2. HRTEM lattice image of the pillared clay M01,  $\text{Fe}/(\text{Al}+\text{Fe}) = 0.1$ . Two typical domains of the periodic structures are labeled with one arrow for  $[d_{001}]_1 = 1.31 \text{ nm}$  and with two arrows for  $[d_{001}]_2 = 1.52 \text{ nm}$ , respectively.

Figure 1. XRD traces of different pillared montmorillonites.

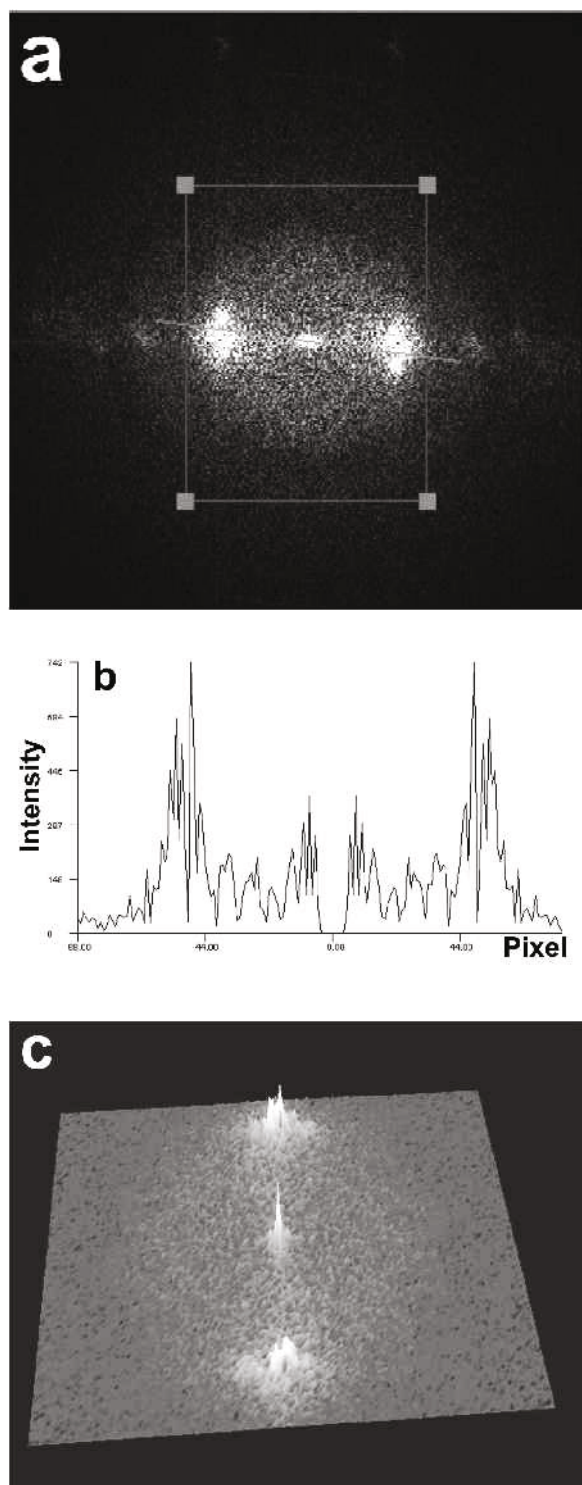


Figure 3. 2D Fourier transform of Figure 2. (a) Amplitude modulus ('mo'); (b) profile of reflections in 'mo' image along the  $x$  axis with 1 pixel =  $8.6 \times 10^{-2} \text{ nm}^{-1}$ . The central peak of the 'mo' image has been erased; (c) 3D visualization of the zone inside the rectangle outlined in white in part a.

Figure 3b shows high fluctuations in intensity and therefore cannot be used for a precise determination of the diffraction maximum positions. These fluctuations are not real diffraction peaks but only fluctuations of the gray level in each pixel. Such a curve is essential for selecting the dimensions of the filter mask needed to isolate the extension domains of the diffraction peaks, but it cannot be used to label them directly.

The image in Figure 3c is the 3D visualization of the zone inside the rectangle (outlined in white in Figure 3a). It confirms the presence of only two distinct diffraction peaks indicating two different periodic arrangements in the lattice image of this sample (Figure 2).

#### Filter mask selection

The filtration process is performed by fitting a filter to the 'mo' image as shown in Figure 4a. We have used a ring-shaped filter with a minimum limit  $q_{\min} = 3.43 \text{ nm}^{-1}$  and the maximum limit  $q_{\max} = 1.44 \text{ nm}^{-1}$ . These limits were selected on the basis of a series of tests carried out to optimize the contrast of the lattice fringes (Figure 4b). In this case the low frequencies in the central beam are hidden. This eliminates the large-scale intensity fluctuations permitting an homogeneous contrast to be obtained throughout the whole image. However, the filter cut off by  $q_{\max}$  in the 'mo' image could also give rise to secondary oscillations in the lattice fringes after the second Fourier transform applied to restore the direct image. This effect was greatly reduced by smoothing the step profile of the ring filter edges by convolution with a 2D Gaussian function. This convolution uses an algorithm (all the algorithms used in

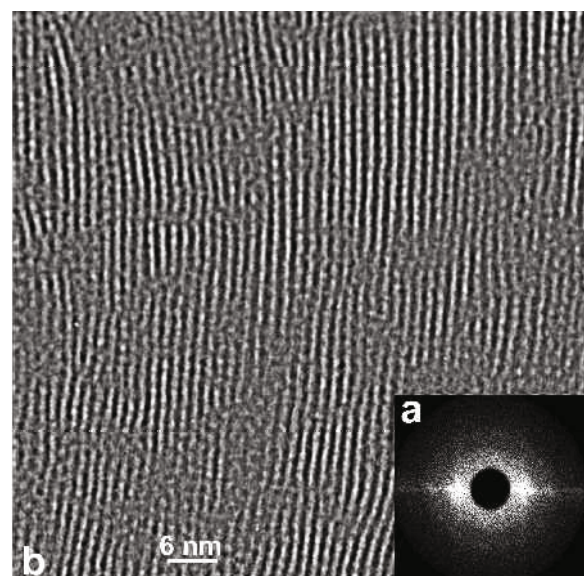


Figure 4. (a) Filter mask adjusted on 'mo' image; and (b) lattice image of M01 after Fourier transformation of part a.

this work were built from the 'Visilog' program functions provided by the Noisis company) allowing the selection of the decrease rate of the smoothing function adapted to the contrast between the noise background and the lattice fringes.

In Figure 4, the extensions of ordered domains and of their disordered boundaries are much better defined than in the starting image (Figure 2), but information is still lacking about the distribution, within these domains, of the two basal spacings expected from the splitting of the diffraction peaks (Figure 3c).

After this first cleaning of the image, it is possible to analyze the homogeneity of periodicity in the various ordered domains. By selecting adequate limits for the filter mask it is possible to separate the two types of interlayer spacings.

Figure 5a shows the filtered lattice fringes after the use of a ring-shaped filter (limited by  $q_{\max} = 5.31 \text{ nm}^{-1}$  and  $q_{\min} = 4.29 \text{ nm}^{-1}$ ) which only selects one of the two

diffraction peaks, as shown in the shaded zone of Figure 5b. Figure 6a shows the other fringe family for a filter limited by  $q_{\max} = 4.29 \text{ nm}^{-1}$  and  $q_{\min} = 3.45 \text{ nm}^{-1}$  corresponding to the selection of the second diffraction peak.

The selected ring-filter widths in Figures 5a and 6a are equal to  $\Delta q$  ( $q_{\max} - q_{\min}$ ) = 1.02 and 0.86, respectively. Taking into account the relatively limited size of the diffraction spots, the application of these filters is equivalent to performing a direct image convolution by a step function ( $\sin x/x$ ) whose mean widths at half-height ( $\Delta r = 2\pi/\Delta q$ ) are 6.15 and 8 nm. Such an operation has no effect on the most ordered parts of image on account of filter-edge smoothing.

It is worth noting that the residual noise in 'knitting stitch' is observed in the disordered parts of the image and/or in the parts hidden by the filter. This effect is due to the common limit of both filters at  $q = 4.29 \text{ nm}^{-1}$ . This limit corresponds to a cut-off of the diffraction

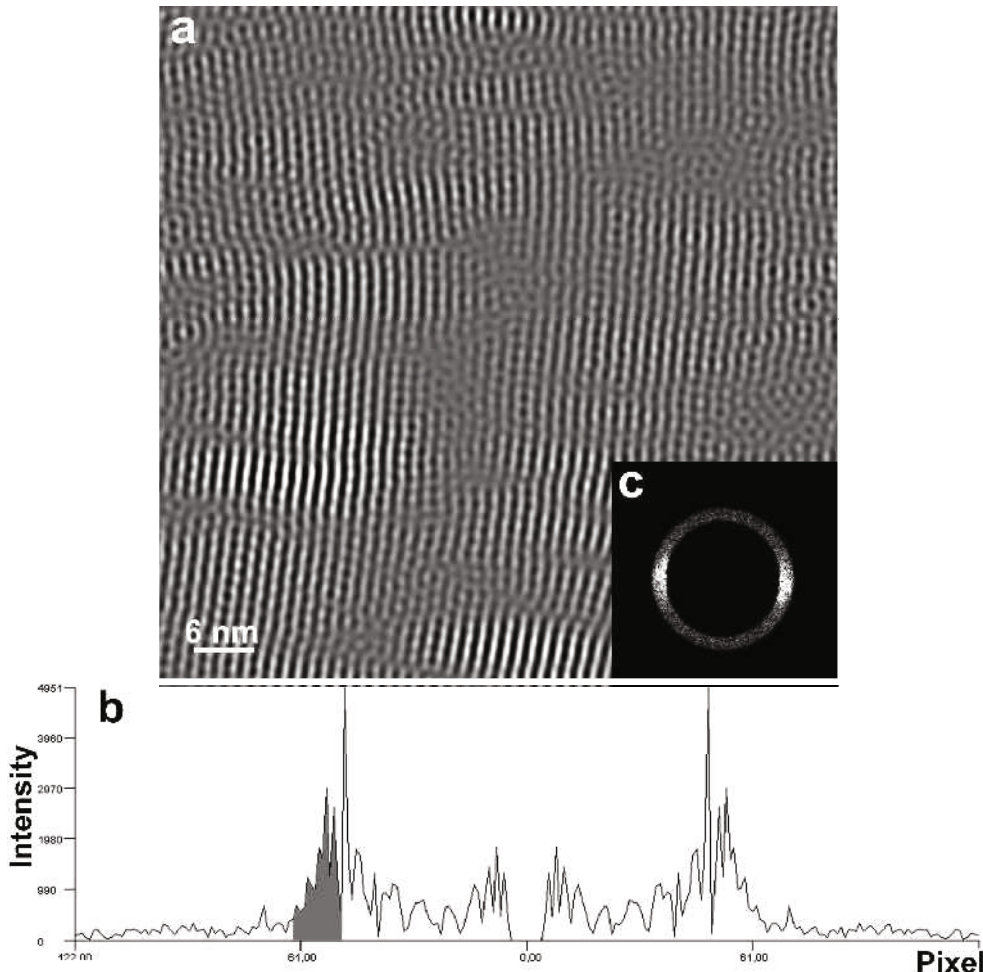


Figure 5. (a) Lattice imaging after Fourier transformation of part c; (b) dark zone showing the limitation of the filter (c) which selects the first reflection.

peaks which are very close (Figures 5b and 6b). The cut-off effect creates circular fringes whose intensity varies as a zero-order Bessel function the first minimum of which is at 1.46 nm (Fourier transform of a circular diaphragm of radius 4.29 nm<sup>-1</sup>).

Of most interest in Figures 5a and 6a, is the differentiation of the two species of ordered domains characteristic of each layer-stacking period.

However, the images so obtained still do not permit easy quantitative measurements of the interlayer distances. It is now necessary to obtain homogeneous fringe profiles with constant width which should be as narrow as possible. A two-step procedure is applied which includes a 'top hat' transformation followed by the classical skeletonization.

#### 'Top hat' transformation and skeletonization

The 'top hat' transformation consists of changing the Gaussian profile of the lattice fringe cross-section into a 'top hat' profile via a number of iterations, including a

dilatation function followed by an erosion function, which are applied to the white fringes profile. Such a transformation converges towards homogenization of the gray-level distribution along the fringes (Figures 5a–7).

The classical method of skeletonization reduces the fringe width to a single pixel. Both types of ordered domains are together again in Figure 8. In these domains, the interlamellar distances are very regular and can be measured by one pixel (the pixel width is 0.046 to ~0.050 nm). Such precision only means a very small interlayer distance fluctuation within the stackings. It cannot be related to the specific resolution of the TEM image (0.14 nm) which represents the discrimination distance between two points. The distances measured in Figure 8 are [ $d_{0011}$ ] = 1.31 ± 0.025 nm and [ $d_{001}2$ ] = 1.52 ± 0.025 nm, respectively. It is worth noting that there is some overlap in the spread of the two distances. These anomalies are related to the overlap of both diffraction peaks. This is caused by the need to have a common limit for both filters to separate the two

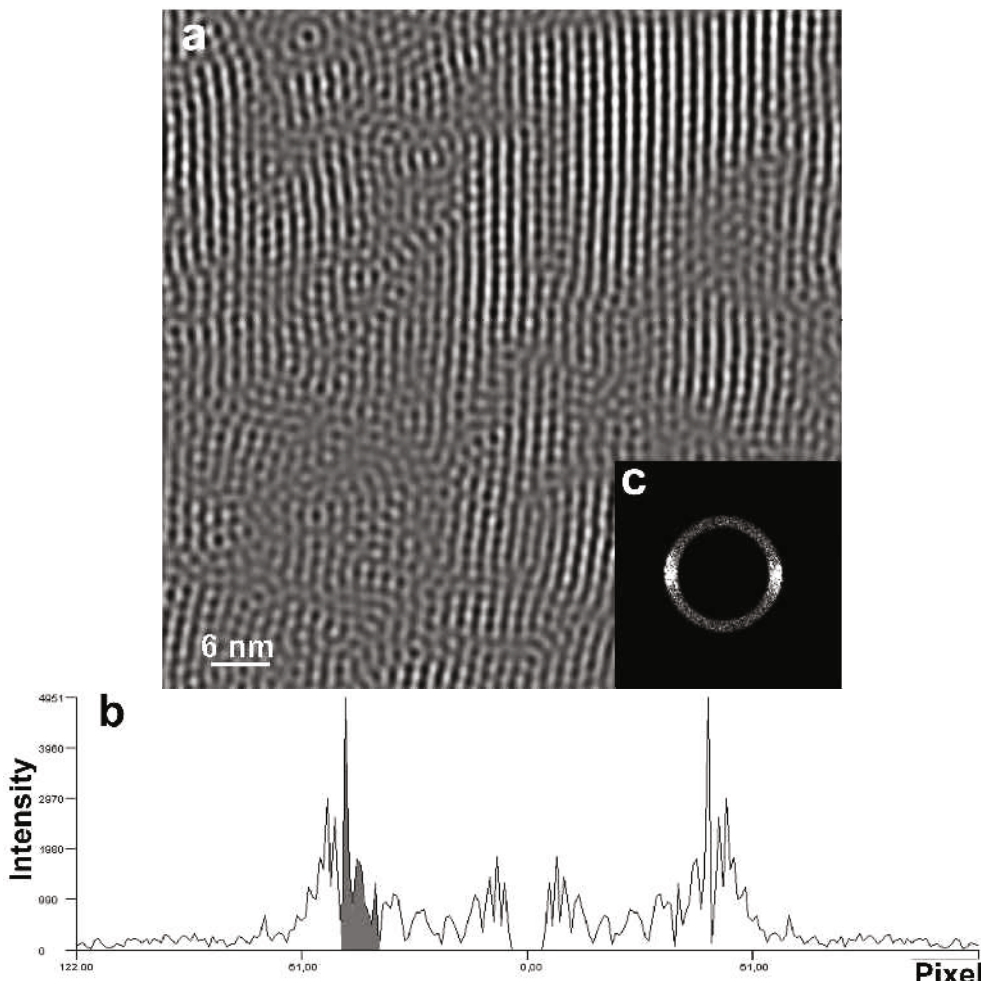


Figure 6. (a) Lattice imaging of M01 after Fourier transformation of part c; (b) dark zone showing the filter (c) which selects the second reflection.

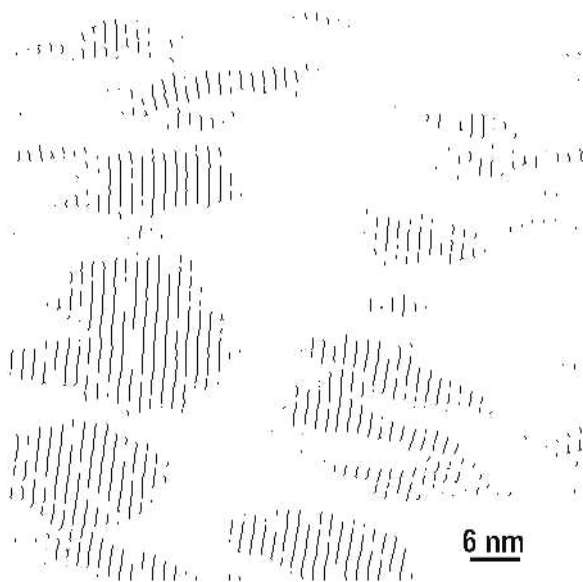


Figure 7. Lattice imaging after the 'top hat' transformation of Figure 5a.

periodicities. This induces an inability to determine the limits of the two Fourier transforms and therefore the boundaries of the ordered domains as seen in Figures 5 and 6.

## RESULTS

### Sample M05

The TEM image of M05 shows that this mixed Al-Fe pillared clay consists of ordered stacked layers alternating with globular phases and mesoporous spaces. Numerous TEM images were recorded to assess the homogeneity of pillaring in this sample. Figure 9 shows the most significant digitized image of this sample. It is composed of particles containing a variable and rather small number of layers. These particles are separated from each other by regular mesopores, containing uncompacted aggregates of Fe oxide nodules.

*Layer stacking analysis.* The Fourier transform of the image in Figure 9 is shown in Figure 10a. As previously described, the filtration procedure which was applied to the diffraction peak in Figure 11 revealed a wide distribution of basal spacings with a mean value [ $d_{001}$ ]  $\approx 1.58 \pm 0.10$  nm. A regular spacing of  $1.22 \pm 0.025$  nm was measured for the greatest layer stacking observed at the top of the image (Figure 9).

*Small-angle scattering analysis.* The diffraction image (Figure 10a) shows a diffuse small-angle scattering spot. This is due to the presence of large-scale heterogeneities of matter observed in the sample (Figure 9) with respect to mesopores and aggregates of Fe oxide nodules. In an attempt to explain the origin of the diffraction maximum

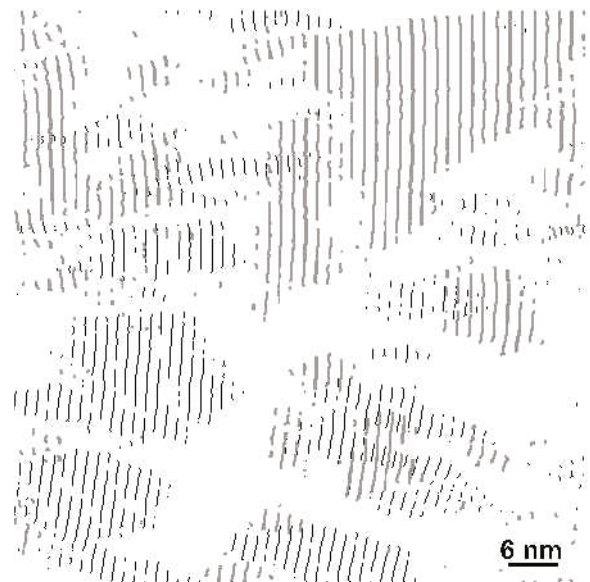


Figure 8. Lattice imaging after skeletonization of Figure 7 and superposition of the same image resulting from Figure 6a. This second fringe family has been darkened to make the two periodicities distinct.

at 7.2 nm (Figure 1), a filter mask was selected to erase all the details of the layered structure, keeping only the details larger than the biggest basal spacing.

The mask chosen was an annular filter with an external radius

$$q_{\max} = 2.86 \text{ nm}^{-1} (= 2\pi/2.2 \text{ nm})$$

and an internal radius

$$q_{\min} = 0.25 \text{ nm}^{-1} (= 2\pi/25.1 \text{ nm})$$

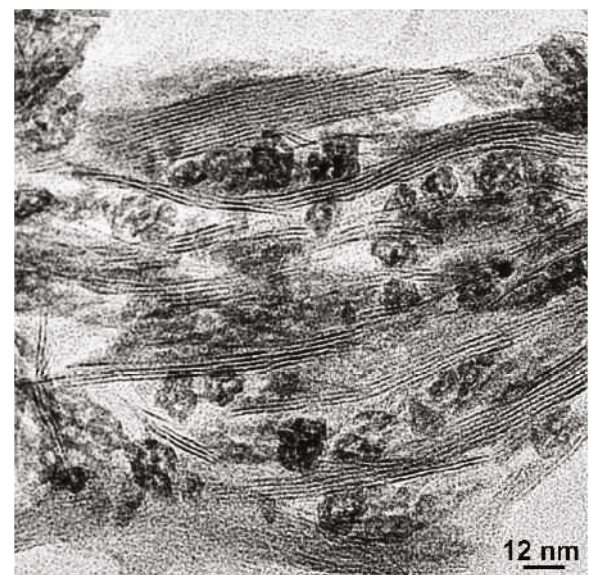


Figure 9. HRTEM lattice image of pillared montmorillonite M05: Fe/(Fe+Al) = 0.5.

which has been smoothed following the procedure described in the section on 'Filter mask selection'. The result of the filtration is shown in Figure 11. If this image is compared with the original (Figure 9) two effects are observed: (1) a negative effect due to the introduction of a cut-off by the limitation of  $q_{\max}$ . Indeed, the scale of the layered structure and that of the density heterogeneities are not really distinct. As shown in Figure 10(a,b) there is a continuum between the diffraction and the small-angle scattering domains. The

consequence is an ambiguity in the measurement of the unit nodule size and the cut-off of the filter. (2) A positive effect due to enhancement of contrast between the Fe nodules and the porosity of the clay and clarification of the internal arrangement within the nodule aggregates. Although individual Fe oxide nodules have the same size, the resulting aggregates have varied configurations: as linear arrangements between two clay layers or as rings with the number of rings changing from one aggregate to other. A comparison of

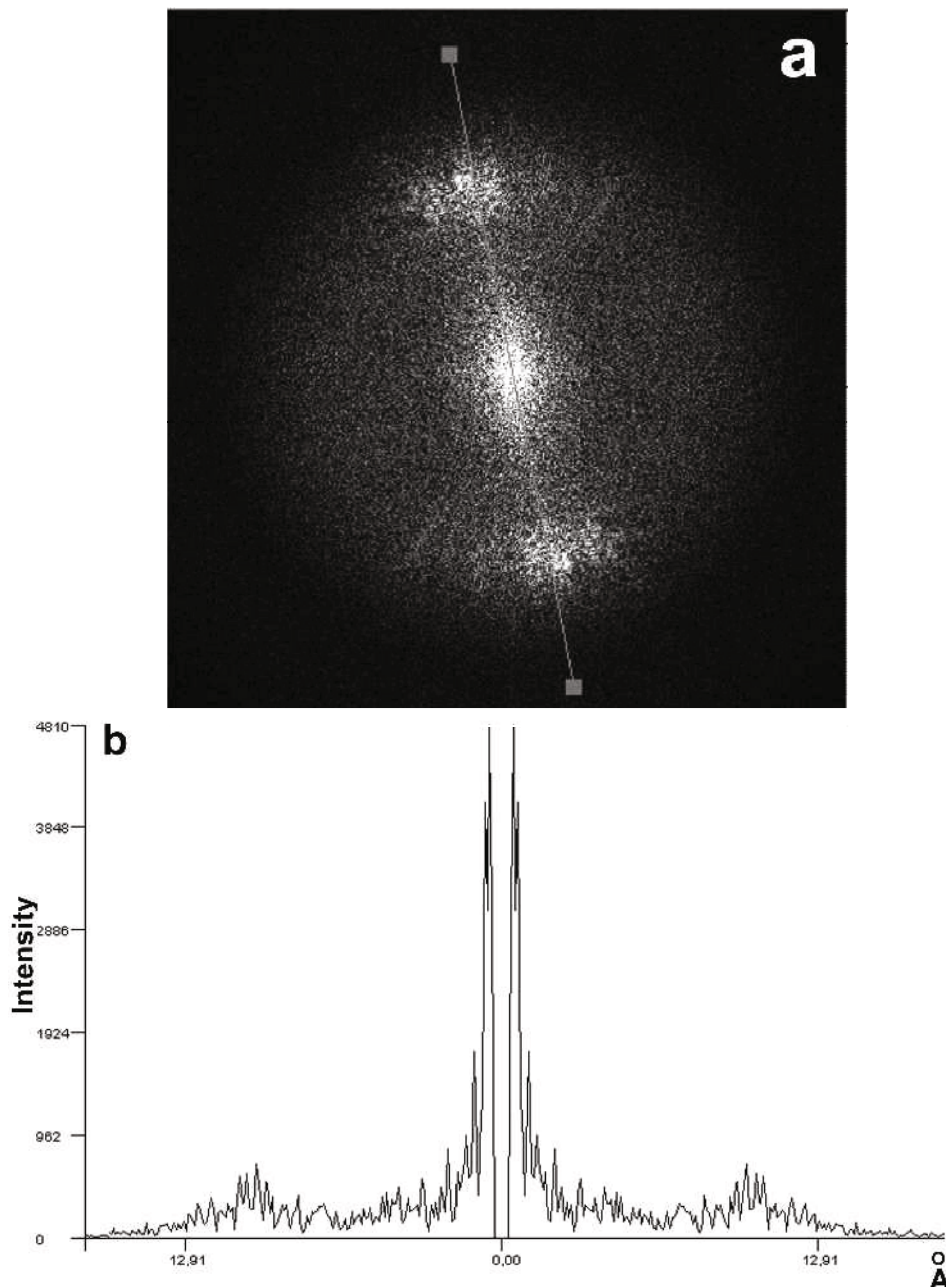


Figure 10. 2D Fourier transform of Figure 9. (a) Amplitude modulus 'mo' and (b) profile of reflections of 'mo' image along the values along the x axis are directly calibrated ( $\text{\AA}$ ). We recall that  $x = q (\text{\AA}^{-1}) = 2\pi/d$  in which  $d$  is in  $\text{\AA}$ .

Figures 9 and 11 shows that the Fe aggregates have three sizes (Figure 12). The diameter of the first unit nodules is ~1.6 nm, as observed by Tchoubar *et al.* (1991). The second size is that of spherulitic clusters formed by nodule condensation, with a diameter of ~3.8 nm. The third size is given by aggregates of variable shape and a thickness or diameter of ~7.0 nm. The lenticular mesopores which appear in these pillared clays, with thicknesses varying from 2.5 to 50 nm, result from aggregate intercalation.

It is worth noting that the aggregate diameter (thickness) is ~7.0 nm, the same size as determined from the XRD peak position (at 7.2 nm). This observation, however, does not provide adequate justification for the presence of the diffraction peak. In order to obtain an explanation, a narrow filter mask was adjusted progressively to hide the details of the internal structure of the aggregates, keeping only their external shell. This operation was successful when the filter was adjusted to  $q = 0.45 \text{ nm}^{-1}$ . It is indeed possible to obtain a threshold image in black and white (Figure 13), with the white parts corresponding to the distribution of volumes in which the Fe oxide aggregates are included. This  $q$  value corresponds to a correlation distance of ~14 nm in the direct space, about twice 7.2 nm.

## DISCUSSION AND CONCLUSION

The treatment of HRTEM images, as used in this work, was applied for the first time here to the study of clay minerals.

It shows that the periodic structures of mixed Al-Fe pillared montmorillonite are complex. Analysis of the

diffraction peaks, after Fourier transform of the direct image, has revealed the presence of domains of different layer stackings, and with different chemical compositions of the interlayer species. The chemically homogeneous domains have lateral extensions (some tens of nm) smaller than the size of the montmorillonite layer (some hundred of nm). The intercalation process therefore involved various chemical species within a single interlayer space. As the starting solutions of Fe and Al do not have the same pH, their mixing can induce a partial decomposition of the  $\text{Al}_{13}$  polymer giving rise to smaller oligomers (dimers or trimers). The same effect can occur with the Fe polymers under the influence of Al ions. Indeed, in sample M01 (Figure 2) which contains a small proportion of Fe ions, the 1.31 nm basal spacing could correspond to intercalation of an Al oligomer other than  $\text{Al}_{13}$ . The 1.52 nm distance, probably due to the intercalation of an Fe oligomer, is maintained when the proportion of Fe ion increases.

With respect to sample M05 (Figure 10) containing a larger proportion of Fe than M01, the large range of basal spacings is certainly related to large range of oligomers that can be formed with Fe ions. The 1.22 nm spacing may correspond to the presence of  $\text{Fe}^{3+}$  cations with their first hydration sphere. The 1.58 nm spacing seems more typical of the Fe oligomer. However, it disappears for the sample which no longer contains Al ions (Figure 1).

Analysis of sample M05 also reveals the localization and structure of the iron aggregates. These particles are involved in the formation of mesopores which in turn may give rise to interesting new surface properties.

The most interesting information which could be obtained from this sample is the identification of the 7.2 nm spacing observed by XRD. This observation cannot be attributed to simple intercalation. The origin of this peak, might be explained by a thorough examination of an apparently random image

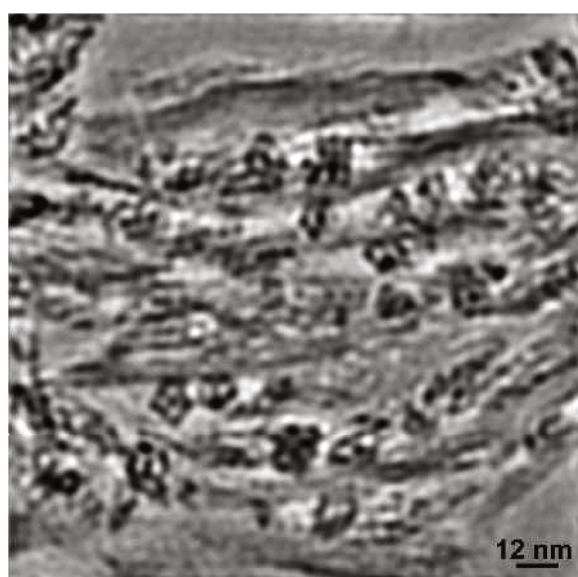


Figure 11. Filtered lattice image of M05 (Figure 9). The limits of the filter are 2.2 nm and 25 nm. Fe particle contrast has been enhanced.

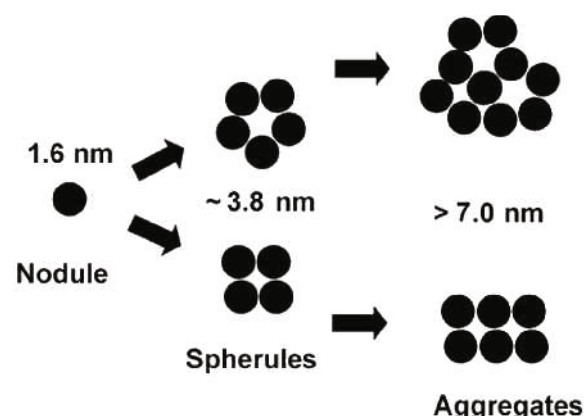


Figure 12. The different scales of Fe aggregates as they are observed in Figures 9 and 11.

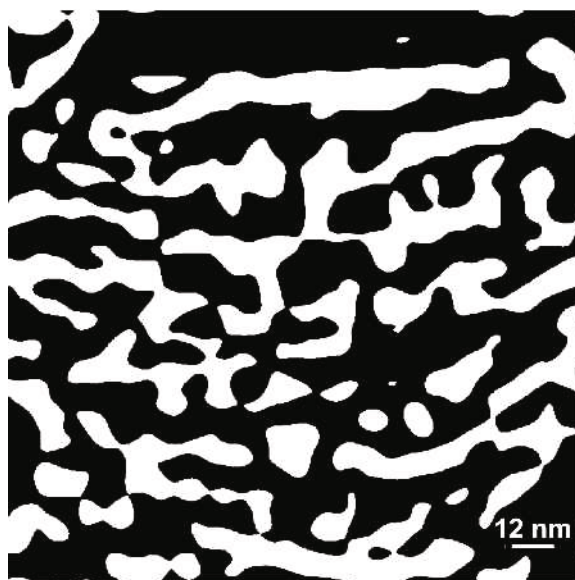


Figure 13. Threshold image after a filter mask which is adjusted on  $q = 0.45 \text{ nm}^{-1} \approx 2\pi/14 \text{ nm}$ .

(Figure 13) showing the volume distribution of the iron aggregates. This type of image has been studied in random porous media by Levitz and Tchoubar (1992). They were able to show that some of these media (e.g. Vycor glass) with highly correlated voids can give a diffraction peak. This peak corresponds to the statistical correlation length as determined from the chords distribution within the black and white domains of the sample. Work in progress is aimed at using this information to simulate the corresponding scattering spectrum.

In summary, image analysis has shown the presence of domains of different layer stackings, with different chemical compositions of the interlayer species. The pillaring process involves various chemical species within a single interlayer space. The most important feature is that the first peak observed by XRD at 7.2 nm for a mixed Al-Fe pillared montmorillonite does not correspond to a classic periodic pillared structure. In addition, the image analysis can account for the presence of mesopores arising from the insertion of globular Fe aggregates into the raw natural clay.

#### ACKNOWLEDGMENTS

We thank Dr Benny Theng of Landcare Research (New Zealand) for valuable comments on the manuscript.

#### REFERENCES

- Bergaya, F. (1990) Argiles à piliers. Pp. 511–538 in: *Matériaux Argileux, Structures, Propriétés, et Applications* (A. Decarreau, editor). SFMC-GFA, France.
- Bergaya, F., Dion, P., Alcover, J.F., Clinard, C. and Tchoubar, D. (1996) TEM studies of kaolinite thermal decomposition by controlled rate thermal analysis. *Journal of Material Science*, **31**, 5069–5075.
- Clinard, C., Rouzaud, J.N. and Pellenq, R.J.M. (2001) Analyse d'images de haute résolution en microscopie électronique par transmission. Application au cas des carbones micro-texturés. Pp. 29–34 in: *V.I.M Conference Proceedings*, Nancy, France.
- d'Emmerez de Charmoy, R., Mari, D., Barrault, J., Zivkov, C., Van Damme, H., Hassoun, N., Bergaya, F., Setton, R. and Gatineau, L. (1987) Patents FR 87 09 763 and FR 87 09 764 Procédé de préparation de nouveaux catalyseurs à base de montmorillonites et/ou de laponites pontées pour la conversion sélective du gaz de synthèse.
- Douce, N., Djebaili-Chaumeix, N., Paillard, C.E., Clinard, C. and Rouzaud, J.N. (1999) Pyrolysis and oxidation of toluene behind reflected shock waves. Pp. 251–258 in: *Proceedings of 4th International Conference on Combustion, Energy, Experiments and Modeling*, Capri, Italy.
- Fompérie, L., Amigouet, P., Bergaya, F. and Mandalia, T. (2000) Patent FR 00 07 017 Nanocomposites à base d'argile pontée et pontée organo et câble contenant un tel nanocomposite.
- Fompérie, L., Amigouet, P., Bergaya, F. and Mandalia, T. (2001) Patent EP 1 160 277 A1. *A nanocomposite based on a bridged clay, and a cable, comprising said composite*.
- Levitz, P. and Tchoubar, D. (1992) Disordered porous solid: From chord distribution to small angle scattering. *Journal of Physics*, **2**, 771–790.
- Mandalia, T., Messad, D., Crespin, M. and Bergaya, F. (1998) Large interlayer repeat distance observed for montmorillonite treated by mixed Al-Fe and Fe pillaring solutions. *Chemical Communications*, 2111–2112.
- Mandalia, T., Clinard, C. and Bergaya, F. (2003) Mesoporous smectites obtained by addition of Al and Fe pillaring solutions. *Microporous and Mesoporous Materials* (submitted).
- Rouzaud, J.N. and Clinard, C. (2003) Quantitative high resolution transmission electron microscopy. A promising tool for carbon material characterisation. *Fuel Processing Technology* (in press).
- Rouzaud, J.N., Galvez, A., Beyssac, O., Fontugne, C., Clinard, C. and Goffé, B. (1999) The multiscale organisation of carbon materials. Pp. 25–28 in: *Proceedings of the 10th International Conference on Coal Science*, Taiwan.
- Sharma, A., Kyotani, T. and Tomita, A. (1999) A new quantitative approach for microstructural analysis of coal char using HRTEM images. *Fuel*, **78**, 1203–1212.
- Tchoubar, D., Bottero, J.Y., Quienne, P. and Arnaud, M. (1991) Partial hydrolysis of ferric chloride salt: Structural investigations by Photon Correlation Spectroscopy and Small Angle Scattering. *Langmuir*, **7**, 398–402.

(Received 21 May 2002; revised 6 March 2003; Ms. 662)